This paper appears in Journal of Medical Robotics Research, 2024.
https://doi.org/10.1142/S2424905X24500041

Journal of Medical Robotics Research, Vol. 0, No. 0 (2024) 1–15

Robotic Assistance and Haptic Feedback in Arthroscopic Procedures: Design and Preliminary Evaluation of a Two-Arm System

Teng Li[a], Armin Badre[b,c], Mahdi Tavakoli[a]

[a] *Department of Electrical and Computer Engineering, University of Alberta, Edmonton T6G 1H9, Alberta, Canada*
E-mail: {teng4, mahdi.tavakoli}@ualberta.ca

[b] *Western Hand & Upper Limb Facility, Sturgeon Hospital, St. Albert T8N 6C4, Alberta, Canada*
E-mail: badre@ualberta.ca

[c] *Division of Orthopaedic Surgery, Department of Surgery, University of Alberta, Edmonton T6G 2R7, Alberta, Canada*

ABSTRACT: Robot-assisted arthroscopic surgery has been receiving growing attention in the field of orthopedic surgery. Most of the existing robot-assisted surgical systems in orthopedics place more focus on open surgery than minimally invasive surgery (MIS). In traditional arthroscopic surgery, the surgeon needs to hold an arthroscope with one hand while performing the surgical operations with the other hand, which can restrict the dexterity of the surgical performance and increase the cognitive load. On the other hand, the surgeon heavily relies on the arthroscope view when conducting the surgery, whereas the arthroscope view is a largely localized view and lacks depth information. To assist the surgeon in both scenarios, in this work, we develop a two-arm robotic system. The left-arm robot is used as a robot-assisted arthroscope holder, and it can hold the arthroscope still at a designated pose and reject all other potential disturbances, while also allowing the operator to move it via a pedal switch whenever needed. The left-arm robot is implemented with an impedance controller and a gravity iterative learning (Git) scheme, where the former can provide compliant robot behavior, thus ensuring a safe human-robot interaction, while the latter can accurately learn for gravity compensation. The right-arm robot is used as a robot-assisted surgical tool, providing virtual fixture (VF) assistance and haptic feedback during the surgery. The right-arm robot is implemented with a point-based VF algorithm, which can generate VF directly from point clouds in any shape, render force feedback, and deliver it to the operator. Furthermore, the VF, the bone, and the surgical tool position are visualized in a 3D digital environment as additional visual feedback for the operator. A series of experiments are conducted to evaluate the effectiveness of the prototype. The results demonstrate that both arms can provide satisfactory assistance as designed.

Keywords: Robot-assisted surgical system; arthroscopic surgery; two-arm robot system; iterative learning; gravity compensation; impedance control; virtual fixture; haptic feedback; physical human-robot interaction.

1. Introduction

Robotic systems and techniques for orthopedic surgery have been developed and evolved for several decades.[1] Nowadays, robot-assisted surgical systems have predominated over many orthopedic surgeries, such as total hip arthroplasty (THA), total knee arthroplasty (TKA), unicompartmental knee arthroplasty (UKA), and spine surgery.[1] On the other hand, robot-assisted minimally invasive surgery (MIS) has received more and more attention in orthopedics and beyond due to its advantages of a faster recovery rate and decreased pain.[2] However, most of the existing robotic systems in orthopedics have more focus on open surgery than MIS like arthroscopic surgery.[1,2]

Elbow arthroscopy is a common arthroscopic surgery in orthopedics that is commonly used for the management of elbow arthritis, stiffness, tendinosis, fractures, and instability in a minimally invasive fashion.[3] During traditional elbow arthroscopy, the surgeon needs to hold an arthroscope with one hand while conducting the surgery with the other hand under the arthroscope view. The arthroscope view may need to be adjusted many times during the surgery in order to observe the surgical site from different perspectives or change to another surgical site. Holding the arthroscope still is important for the surgeon to conduct the surgery smoothly since the arthroscope view is the main visual feedback the surgeon relies on to visually observe and locate the surgical site, but this could make the surgeon easy-to-fatigue and high cognitive load thus have adverse effect on the surgical performance. This arouses the neces-

sity to develop a robot-assisted system where the robot can hold the arthroscope still for the surgeon, which can free the surgeon's hand for other more important tasks, *e.g.*, replacing the surgical bur with another one in a different shape.

To build a robotic assistant as an arthroscope holder, some requirements need to be met.[4] First, The robot can hold the arthroscope still at a fixed position while rejecting all possible disturbances (*e.g.*, external disturbances delivered to the arthroscope via contact with the patient's body during surgery). This will ensure the surgeon always receives stable visual feedback even when some occasional disturbances are delivered to the arthroscope. Second, when the surgeon needs to move the arthroscope to adjust the scope view perspective or to a new surgical site, the robot should enable physical human-robot interaction (*p*HRI) and allow the arthroscope to be moved around freely. The main concerns in building such a robot-assisted arthroscope holder are the dynamic model uncertainties and external disturbances, which could largely affect the robot's performance accuracy and even stability if they are not appropriately compensated for in the robot dynamics. More specifically, incomplete gravity compensation can be the main issue since heavy external surgical tools (*e.g.*, the arthroscope) will be attached to the robot end-effector (EE).

In the two-arm system proposed in this work, the left-arm robot will be designed as a robot-assisted arthroscope holder to satisfy the requirements described above. It will mainly tackle the problem of disturbance estimation and gravity compensation while ensuring a robust and safe human-robot interaction. To this end, we have explored different approaches including disturbance observer, neural network (NN), and gravity iterative learning (Git) scheme in our previous work.[4–6]

Disturbance observer is a promising way to estimate and compensate for dynamic uncertainties including gravity. In our previous work,[4] we have shown that by integrating impedance control and nonlinear disturbance observer, an accurate impedance control can be achieved. In that work, the disturbance observer can accurately estimate and compensate for the lumped uncertainties including incomplete gravity compensation. However, the problem is that the nonlinear disturbance observer (NDOB) as well as any other types of observers, such as generalized momentum observer (GMO), joint velocity observer (JVOB), extended state observer (ESO), and disturbance Kalman filter (DKF) method, always estimate all the uncertainties as a lumped term and is not able to separate any one component out.[4,7] Moreover, the observer will refuse human-robot interaction since human-applied force will also be taken as a part of the lumped disturbances thus being rejected.[4] Then, we tried to use an NN model to learn and separate a specific component from the uncertainties.[5] Although it works well, it requires tremendous data and time to train the NN model before use. To solve the problem more efficiently, we developed a gravity iterative learning (Git) scheme in [6], especially for gravity compensation since the gravity of the external surgical tools attached to the robot EE is the main issue in our application scenario. With the Git scheme, the uncompensated gravity can be accurately learned and compensated for in an online manner.

In the left-arm robot-assisted arthroscope holder, an integrated framework of integrating an impedance controller and the Git scheme will be implemented. The impedance controller will ensure compliant robot behavior thus a robust and safe human-robot interaction. The Git scheme will iteratively learn and compensate for the gravity in the robot dynamics thus ensuring an accurate and stable robot control system, and also enable human-robot interaction via a pedal switch when necessary.

On the other hand, it could be helpful for surgeons by providing them with additional haptic feedback via virtual fixture (VF). In the field of robot-assisted surgery, VF has been widely used due to many potential benefits, such as reducing the surgeon's cognitive load,[8] improving surgeon's surgical performance,[9] and making the surgical outcome more accurate and safe. Park *et al.* conducted a preliminary test on VF in a blunt dissection task.[10] Their results indicated faster and more precise task performance with the VF-assisted method than the conventional free-hand method. Ryden *et al.* developed a method to generate VF directly from point cloud to protect the beating heart during surgery.[11] They improved their method further in [12,13].

The haptic VF has been playing a vital role during various surgical procedures in robot-assisted surgery, such as suturing,[14] knot tying,[8] dissection,[15] either assisting in moving the surgical tool along a trajectory or preventing it from entering a specific area for protecting the objects inside (*e.g.*, beating heart or nerve).[11,16] Many research works have proved that VF with haptic feedback can provide effective help to improve performance in surgical tasks. Johansson *et al.* evaluated the feasibility and repeatability of using haptic VF to guide fibula osteotomies in mandible reconstruction surgery.[17] As a further step, Cheng *et al.* proposed a robotic assistant incorporating augmented reality (AR) visualization and haptic VF for fibula osteotomies in mandible reconstruction surgery.[18] By comparing several methods on the same fibula osteotomy task, their results showed that with the help of AR and VF, the task precision can be improved.

In orthopedics, surgical plans are usually made based on preoperative images of a patient. For example, determining the location and amount of osteophytes to be debrided or the location of critical neurovascular structures to be avoided. In traditional arthroscopic surgery, as mentioned earlier, the surgeon heavily relies on the visual feedback from the arthroscope view to perform the surgical procedures at hand. Also, the surgeon may need to mental image the surgical site and conduct the surgical procedure (*e.g.*, removing the osteophytes) by intuition and experience since the arthroscope view is largely localized and lacks of depth information. A robot-assisted surgical tool (*e.g.*, a surgical bur) with haptic assistance can be designed to relieve this problem, *e.g.*, to help the surgeon reduce the mental load by

providing additional visual feedback and haptic feedback. To this end, some curves can be drawn in the preoperative images to mark out boundaries of removing osteophytes, or of protecting nerves inside. Then, with a robotic system, the hand-drawn curves or the patient's bone in the preoperative images can be used to generate VF which can assist in removing osteophytes or protecting the nerves by providing haptic feedback. However, the hand-drawn curves or the bone are usually in irregular shapes which may not be able to be presented mathematically by equations that are often required by most existing VF generating algorithms. To solve this problem, we developed a point-based VF generation algorithm in [19], which allows us to generate VF directly from point clouds in any shape.

Therefore, the right-arm robot in the proposed two-arm system will be designed to be a robot-assisted surgical tool with haptic feedback from VF, where the VF can be generated directly from point clouds in any shape, *e.g.*, a hand-drawn curve, or a patient-specific bone model. Furthermore, augmented 3D visual feedback will be provided to the surgeon to indicate the generated VF and the real-time location of the surgical tool in a more global view in addition to the localized arthroscope view.

In summary, by integrating our previous work together,[4,6,19] a prototype of a two-arm robot-assisted arthroscopic surgical system is designed and experimentally evaluated in this paper. The left-arm robot, a robot-assisted arthroscope holder, is implemented with an integrated framework of impedance control and Git scheme developed in [6], which can ensure a safe human-robot interaction while accurately learning for gravity compensation. The left-arm robot can help to hold the arthroscope still at a designated pose and also allow the operator to move it freely via a pedal switch whenever necessary. The right-arm robot, a robot-assisted surgical tool, is implemented with a point-based VF generation algorithm developed in [19], which can provide VF assistance with haptic feedback to assist the operator in performing surgical operations. Moreover, the VF, the surgical tool, and the force feedback values are visualized in a 3D digital environment to provide the operator with additional visual feedback during the surgery. A series of experiments are conducted to evaluate the effectiveness of the prototype. The main contributions of this paper are described as the following,

(1) A two-arm robot-assisted system (6DOF + 6DOF) is designed and assembled for arthroscopic surgery, while the control systems consist of techniques developed in our previous work.
(2) The effectiveness of each arm is experimentally evaluated and verified, respectively.

This paper builds upon our prior work by not only refining the individual technologies but also demonstrating their synergistic operation within a dual-arm robotic system. The integration of a Git scheme for the arthroscope-holding arm and a point-based VF algorithm for the tool-operating arm presents an advancement that addresses a gap in arthroscopic surgery: the need for a comprehensive system that enhances the surgeon's dexterity and cognitive focus. By unifying these technologies within a single and cohesive framework, we provide a solution that mitigates the cognitive load on surgeons, offering both enhanced stability for the arthroscope and intuitive haptic guidance for the surgical tool.

The remaining paper is organized as follows. Section 2 briefly introduces the impedance controller, the Git scheme, the VF algorithm, and the prototype as well as the control block diagram. Section 3 presents more details about the prototype of the two-arm system design, experimental evaluations, and corresponding results. Section 4 remarks the conclusions.

2. Methods

Robot dynamics governs the motion of a robot in response to external forces or disturbances. Without properly handling the external disturbances (*e.g.*, the mass of the surgical tool attached to robot EE) in robot dynamics, the robot may perform inaccurately or even have unstable or dangerous behavior. In this section, we will first introduce the robot dynamics and disturbances, then we introduce impedance control which can provide compliant robot behavior, and then we introduce a Git scheme that can accurately compensate for external disturbances, especially gravity. At the end of this section, a prototype of the proposed two-arm robot-assisted arthroscopic surgical system will be presented, as well as the control block diagram.

2.1. *Left-Arm: Robot Dynamics and Disturbances*

A general dynamic model for an n-degree-of-freedom (DOF) rigid robot with revolute joints[20] can be given by

$$\underbrace{\mathbf{M}(\mathbf{q})}_{\hat{\mathbf{M}}+\Delta\mathbf{M}}\ddot{\mathbf{q}}+\underbrace{\mathbf{S}(\mathbf{q},\dot{\mathbf{q}})}_{\hat{\mathbf{S}}+\Delta\mathbf{S}}\dot{\mathbf{q}}+\underbrace{\mathbf{G}(\mathbf{q})}_{\hat{\mathbf{G}}+\Delta\mathbf{G}}+\boldsymbol{\tau}_{\mathbf{fric}}(\dot{\mathbf{q}})=\boldsymbol{\tau}+\underbrace{\boldsymbol{\tau}_{\mathbf{ext}}}_{\mathbf{J}^{\mathbf{T}}\mathbf{F}_{\mathbf{ext}}} \quad (1)$$

where $\mathbf{q},\dot{\mathbf{q}},\ddot{\mathbf{q}}\in\mathbb{R}^n$ are the joint position, velocity, and acceleration, respectively, $\mathbf{M}\in\mathbb{R}^{n\times n}$ denotes the inherent inertia matrix, $\mathbf{S}\in\mathbb{R}^{n\times n}$ denotes a matrix of the Coriolis and centrifugal forces, $\mathbf{G}\in\mathbb{R}^n$ represents the gravity vector. $\hat{\mathbf{M}},\hat{\mathbf{S}},\hat{\mathbf{G}}$ represent users' model estimates, while $\Delta\mathbf{M},\Delta\mathbf{S},\Delta\mathbf{G}$ are the corresponding estimate errors. $\boldsymbol{\tau}_{\mathbf{fric}}\in\mathbb{R}^n$ is joint friction, $\boldsymbol{\tau}\in\mathbb{R}^n$ is the commanded joint torque vector, $\boldsymbol{\tau}_{\mathbf{ext}}\in\mathbb{R}^n$ is the torque caused by external force, $\mathbf{F}_{\mathbf{ext}}\in\mathbb{R}^6$ is the external force in Cartesian space, and $\mathbf{J}\in\mathbb{R}^{6\times n}$ is the Jacobian matrix.

By collecting all the disturbances together, the dynamic model (1) of a robot can be re-written as

$$\hat{\mathbf{M}}\ddot{\mathbf{q}}+\hat{\mathbf{S}}\dot{\mathbf{q}}+\hat{\mathbf{G}}=\boldsymbol{\tau}+\underbrace{\boldsymbol{\tau}_{\mathbf{ext}}-[\boldsymbol{\tau}_{\mathbf{fric}}+(\Delta\mathbf{M}\ddot{\mathbf{q}}+\Delta\mathbf{S}\dot{\mathbf{q}}+\Delta\mathbf{G})]}_{\boldsymbol{\tau}_{\mathbf{dist}}} \quad (2)$$

where $\boldsymbol{\tau}_{\mathbf{dist}}$ denotes the lumped uncertainties containing the model error ($\Delta\mathbf{M}\ddot{\mathbf{q}} + \Delta\mathbf{S}\dot{\mathbf{q}} + \Delta\mathbf{G}$), the joint friction $\boldsymbol{\tau}_{\mathbf{fric}}$, and the external disturbances $\boldsymbol{\tau}_{\mathbf{ext}}$.

In our target application, *i.e.*, a robot-assisted arthroscopic surgical system, setpoint regulation and physical human-robot interaction (*p*HRI) are the two main scenarios we are considering. In the steady state of setpoint regulation (*i.e.*, $\mathbf{q} = \mathbf{constant}, \dot{\mathbf{q}} = \ddot{\mathbf{q}} = \mathbf{0}$), it will have, (a) joint friction disappeared, *i.e.*, $\boldsymbol{\tau}_{\mathbf{fric}} = \mathbf{0}$; (b) model error ($\Delta\mathbf{M}\ddot{\mathbf{q}} + \Delta\mathbf{S}\dot{\mathbf{q}} + \Delta\mathbf{G}$) will be reduced to only gravity compensation error ($\Delta\mathbf{G}$); (c) only the gravity of the external constant payloads exists for external disturbances (*e.g.*, the surgical tools attached to the robot EE). By applying these conditions, the dynamic model (1) will become (3).

$$\mathbf{M}\ddot{\mathbf{q}} + \mathbf{S}\dot{\mathbf{q}} + \hat{\mathbf{G}} = \boldsymbol{\tau} + \underbrace{\mathbf{J}^{\mathbf{T}}\mathbf{F}_{\mathbf{ext}} - \Delta\mathbf{G}}_{\boldsymbol{\tau}_{\mathbf{dist}}} \tag{3}$$

The model (3) can be expressed in Cartesian space as

$$\mathbf{M}_{\mathbf{x}}\ddot{\mathbf{x}} + \mathbf{S}_{\mathbf{x}}\dot{\mathbf{x}} + \mathbf{G}_{\mathbf{x}} = \mathbf{J}^{-\mathbf{T}}\boldsymbol{\tau} + \mathbf{F}_{\mathbf{ext}} \tag{4}$$

where $\mathbf{M}_{\mathbf{x}}, \mathbf{S}_{\mathbf{x}}, \mathbf{G}_{\mathbf{x}}$ have

$$\begin{cases} \mathbf{M}_{\mathbf{x}} = \mathbf{J}^{-\mathbf{T}}\mathbf{M}\mathbf{J}^{-\mathbf{1}} \\ \mathbf{S}_{\mathbf{x}} = \mathbf{J}^{-\mathbf{T}}\mathbf{S}\mathbf{J}^{-\mathbf{1}} - \mathbf{M}_{\mathbf{x}}\dot{\mathbf{J}}\mathbf{J}^{-\mathbf{1}} \\ \mathbf{G}_{\mathbf{x}} = \mathbf{J}^{-\mathbf{T}}\mathbf{G} \end{cases} \tag{5}$$

where $\mathbf{M}_{\mathbf{x}}, \mathbf{S}_{\mathbf{x}}, \mathbf{G}_{\mathbf{x}}$ are the $\mathbf{M}, \mathbf{S}, \mathbf{G}$ expressed in Cartesian space, respectively.

2.2. *Left-Arm: Impedance Control*

A desired impedance model[4,21,22] for robot-environment interaction can be expressed as

$$\begin{aligned} \mathbf{F}_{\mathbf{imp}} = \mathbf{M}_{\mathbf{m}}(\ddot{\mathbf{x}} - \ddot{\mathbf{x}}_{\mathbf{d}}) \\ +(\mathbf{S}_{\mathbf{x}} + \mathbf{D}_{\mathbf{m}})(\dot{\mathbf{x}} - \dot{\mathbf{x}}_{\mathbf{d}}) + \mathbf{K}_{\mathbf{m}}(\mathbf{x} - \mathbf{x}_{\mathbf{d}}) \end{aligned} \tag{6}$$

where $\mathbf{M}_{\mathbf{m}}, \mathbf{D}_{\mathbf{m}}, \mathbf{K}_{\mathbf{m}}$ are user-designed matrices for inertia, damping, and stiffness, respectively. Note that $\mathbf{x}_{\mathbf{d}}, \dot{\mathbf{x}}_{\mathbf{d}}, \ddot{\mathbf{x}}_{\mathbf{d}}$ are the desired position, velocity, and acceleration, respectively in Cartesian space, while $\mathbf{x}, \dot{\mathbf{x}}, \ddot{\mathbf{x}}$ are the actual ones. $\mathbf{F}_{\mathbf{imp}}$ is the interaction force between the robot and the environment.

To avoid the measurement of external forces, the designed inertia matrix will be set as the inherent inertia matrix of the robot, *i.e.*, $\mathbf{M}_{\mathbf{m}} = \mathbf{M}_{\mathbf{x}}$. Then, by substituting (6) into (3) with $\mathbf{F}_{\mathbf{ext}} = \mathbf{F}_{\mathbf{imp}}$, the impedance control law can be given by[4]

$$\begin{aligned} \boldsymbol{\tau} = \mathbf{M}\mathbf{J}^{-\mathbf{1}}(\ddot{\mathbf{x}}_{\mathbf{d}} - \dot{\mathbf{J}}\mathbf{J}^{-\mathbf{1}}\dot{\mathbf{x}}_{\mathbf{d}}) + \mathbf{S}\mathbf{J}^{-\mathbf{1}}\dot{\mathbf{x}}_{\mathbf{d}} + \mathbf{G} \\ +\mathbf{J}^{\mathbf{T}}[\mathbf{D}_{\mathbf{m}}(\dot{\mathbf{x}}_{\mathbf{d}} - \dot{\mathbf{x}}) + \mathbf{K}_{\mathbf{m}}(\mathbf{x}_{\mathbf{d}} - \mathbf{x})] \end{aligned} \tag{7}$$

For set-point regulation, *i.e.*, let robot EE stay at a fixed point, it will have $\dot{\mathbf{x}}_{\mathbf{d}} = \mathbf{0}$, $\ddot{\mathbf{x}}_{\mathbf{d}} = \mathbf{0}$. Then, the impedance control law (7) will be simplified and reduced to (8), which is also known as task-space proportional–derivative (PD) controller with gravity compensation.

$$\boldsymbol{\tau} = \mathbf{J}^{\mathbf{T}}[\mathbf{K}_{\mathbf{m}}(\mathbf{x}_{\mathbf{d}} - \mathbf{x}) - \mathbf{D}_{\mathbf{m}}\dot{\mathbf{x}}] + \mathbf{G} \tag{8}$$

With an impedance controller, the robot can behave with compliance and robustness. By tuning the parameters in the impedance model ($\mathbf{K}_{\mathbf{m}}$ and $\mathbf{D}_{\mathbf{m}}$), the robot can be configured to be "soft" or "stiff". And with a "soft" robot behavior, a safe human-robot interaction can be ensured.

2.3. *Left-Arm: Git Scheme*

Since gravity compensation is the main problem in our target application, a gravity iterative learning (Git) scheme is used to solve this problem.[6,23] In our previous work [6], we developed a Git scheme that can accurately learn and compensate for gravity. A brief introduction to the Git scheme will be presented in this subsection, while for more details on the Git scheme please refer to [6]. A Cartesian-space impedance control law (at the i-th iteration, $i = 1, 2, ...$) integrating with the Git scheme for gravity compensation can be expressed by

$$\begin{aligned} \boldsymbol{\tau}_{\mathbf{i}} = \mathbf{M}\mathbf{J}^{-\mathbf{1}}(\ddot{\mathbf{x}}_{\mathbf{d}} - \dot{\mathbf{J}}\mathbf{J}^{-\mathbf{1}}\dot{\mathbf{x}}_{\mathbf{d}}) + \mathbf{S}\mathbf{J}^{-\mathbf{1}}\dot{\mathbf{x}}_{\mathbf{d}} \\ +\mathbf{J}^{\mathbf{T}}[\mathbf{D}_{\mathbf{m}}(\dot{\mathbf{x}}_{\mathbf{d}} - \dot{\mathbf{x}}) + \gamma\mathbf{K}_{\mathbf{m}}(\mathbf{x}_{\mathbf{d}} - \mathbf{x})] + \mathbf{J}^{\mathbf{T}}\mathbf{u}_{\mathbf{i-1}} \end{aligned} \tag{9}$$

where $\mathbf{J}^{\mathbf{T}}\mathbf{u}_{\mathbf{i-1}}$ is an iterative learning term for gravity compensation instead of a gravity term $\mathbf{G}$. For setpoint regulation, it will be reduced to be

$$\boldsymbol{\tau}_{\mathbf{i}} = \mathbf{J}^{\mathbf{T}}[\gamma\mathbf{K}_{\mathbf{m}}(\mathbf{x}_{\mathbf{d}} - \mathbf{x}) - \mathbf{D}_{\mathbf{m}}\dot{\mathbf{x}}] + \mathbf{J}^{\mathbf{T}}\mathbf{u}_{\mathbf{i-1}} \tag{10}$$

The update law for $\mathbf{u}_{\mathbf{i}}$ can be given by

$$\mathbf{u}_{\mathbf{i}} = \gamma\eta\mathbf{K}_{\mathbf{m}}(\mathbf{x}_{\mathbf{d}} - \mathbf{x}) + \mathbf{u}_{\mathbf{i-1}} \tag{11}$$

where $\mathbf{u}_{\mathbf{i}}$ is the iterative learning result at the i-th iteration ($i = 1, 2, ...$), setting $\mathbf{u}_{\mathbf{0}} = \mathbf{0}$ for initialization, γ is a scalar gain, and η is the learning rate with steady-state scaling strategy to enable the iterative learning term updates itself in each sampling loop.[6] The scalar gain γ was mainly used for convergence analysis when the Git scheme was developed in [6], and it is usually set as $\gamma = 1$. According to [6], the learning rate η will first be scaled down from $\eta = 1$ to $\eta = 0.001$ by integrating the steady-state scaling strategy based on the sampling loop (here the sampling loop in our work is 0.001 s), then fine-tuned accordingly.

It is noteworthy that the dynamic model of the specific robot we employed in this work is not available, while in our target surgical scenario, only setpoint regulation and human-robot interaction are needed for the left-arm robot as an arthroscope holder. Therefore, the impedance controller Eq. (8) is sufficient to meet our requirement in this work, which can also avoid involving the dynamic parameters ($\mathbf{M}$ and $\mathbf{S}$). Hence, the integrated control law Eq. (10) is implemented in the left-arm robot.

The major advantages of employing the Git scheme in this work include (1) its simple and compact formulation, (2) its lack of any need for robot dynamics, and (3) its lack of any need for a priori knowledge about the external payloads.[6] The Git scheme will be implemented in the left-arm robot serving as a robot-assisted arthroscope holder. It will address the challenge of maintaining steady tool positioning, or in other words, external disturbances, *i.e.*, uncompensated gravity caused by the mass of the surgical tool attached to the robot EE. Maintaining steady tool positioning, *i.e.*, holding the arthroscope still, is a crucial factor in avoiding surgical errors during delicate arthroscopic procedures, and the Git scheme will help to achieve that.

Moreover, the integrated framework of impedance control and the Git scheme allows human-robot interaction to be enabled via a pedal switch whenever necessary, thus the arthroscope can be moved around to a new arthroscopic view or a new surgical site. It is worth noting that, as illustrated in Fig. 2, the setpoint regulation mode (Interaction Disabled) and the *p*HRI mode (Interaction Enabled) are two interchange behaviors rather than simultaneous. The two modes can be seamlessly switched from one to another in an online manner via a pedal, and the pedal actions are independent of the impedance gains ($\mathbf{K_m}$, $\mathbf{D_m}$), *i.e.* the impedance gains remain unchanged in both modes.

2.4. *Right-Arm: Point-Based VF Algorithm*

To render haptic feedback, a virtual fixture (VF) generation algorithm is required. Most of the existing VF algorithms can deal with the target object with a regular shape by finding out the mathematical representation, but it could be a challenge for the objects with irregular shapes, *e.g.*, a patient-specific bone model, or a hand-drawn curve/surface in a preplan image. Although it still can be processed with some approaches like the god-object algorithm by reconstructing a triangle-meshed model,[24] it could be complicated and time-consuming.

In our previous work [19], we developed a point-based VF generation algorithm that allows us to generate VF directly from point clouds in any regular or irregular shape as long as a set of point clouds of the object can be obtained. The point-based VF algorithm consists of one main algorithm and three embedded algorithms for moving the proxy in different conditions. The effectiveness of the VF algorithm has been evaluated by a series of simulations and experiments. The VF algorithm has also been evaluated successfully in an image-based scenario where a hand-drawn curve in an irregular shape was extracted from an image as a set of point clouds. The VF force is rendered by a simple spring model in the algorithm, and delivered to the operator by the robot as haptic feedback. The details of the point-based VF algorithm are available in [19].

Therefore, the point-based VF generation algorithm will be employed in the right-arm robot. By implementing the point-based VF generation algorithm, VF assistance can be generated and VF force can be rendered. The VF force can assist the surgeon in conducting surgical operations. For example, a VF surface can be set at the bottom of the osteophytes as a boundary, and the surgeon will receive haptic feedback once the surgical tooltip is in contact with the VF surface. The VF assistance and haptic feedback allow for natural hand movements while facilitating precise maneuvers in tight joint spaces.

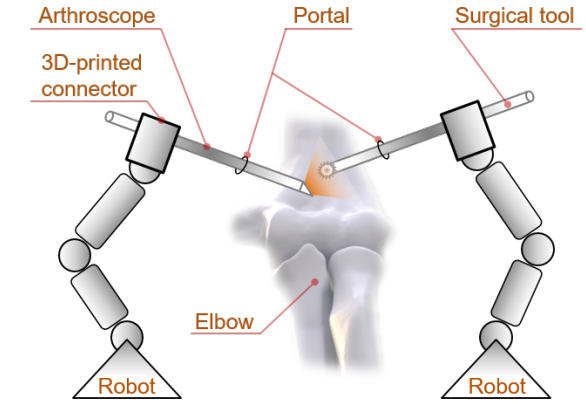

(a) Schematic

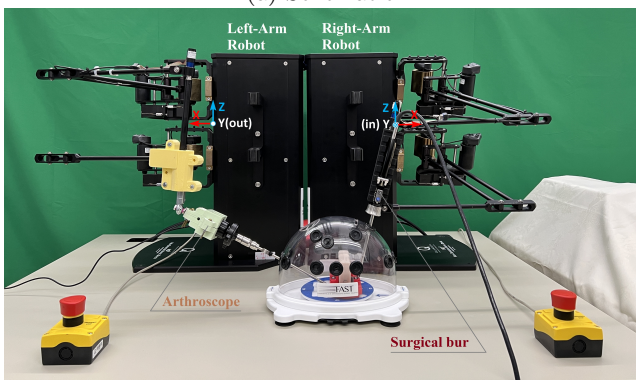

(b) Prototype

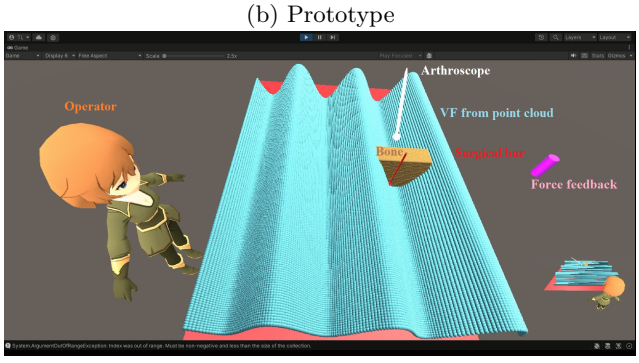

(c) Visualization

Fig. 1: A schematic diagram of the two-arm system in arthroscopic surgery, a prototype of the proposed two-arm robot-assisted arthroscopic surgical system and visualization in Unity. A modified FAST (fundamentals of arthroscopic surgery training) simulator is used as the experimental platform for an arthroscopic surgery mockup.

2.5. *Two-Arm System: Prototype and Control Diagram*

A schematic diagram of robot-assisted arthroscopic surgery is illustrated in Fig. 1a. The schematic diagram serves as a visual summary of the two-arm robotic system's interaction within the surgical environment. Specifically, it illustrates the spatial relationship between the arthroscope, the surgical tool, and the target anatomy (*e.g.*, the elbow). A physical prototype of a two-arm robot-assisted system for arthroscopic surgery is developed as shown in Fig. 1b and Fig. 1c, where Fig. 1b shows the hardware of the prototype while Fig. 1c shows a screenshot of the visualization in Unity. The control block diagram of the prototype system is illustrated in Fig. 2.

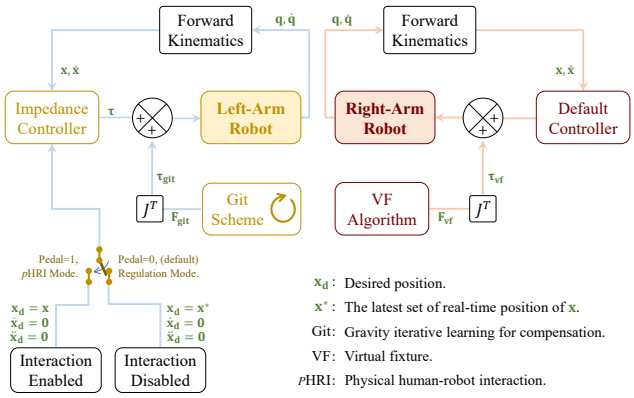

Fig. 2: Control block diagram for the prototype of the two-arm robot-assisted arthroscopic surgical system. When the pedal is pressed ($\mathbf{x_d} = \mathbf{x}$), the position-dependent terms in the impedance controller and the Git update law vanish, whereas the learned result in the Git update law will remain valid, meaning that the *p*HRI mode is activated and interaction is enabled, and now the user can move the robot EE around. When the pedal is not pressed ($\mathbf{x_d} = \mathbf{x}^*$, default), the setpoint regulation mode is recovered and interaction is disabled. Now the Git update law is resumed, and it will continue to learn based on the previous learned result. The latest set of position ($\mathbf{x}^*$) ensures seamless switching between the regulation mode and the *p*HRI mode via the pedal switch.

In the prototype, the left-arm robot has an arthroscope attached to its end-effector (EE), while the right-arm robot has a handheld surgical bur attached to its EE. The left-arm robot is implemented with an impedance controller and a Git scheme. The former can provide compliant robot behavior thus ensuring a safe human-robot interaction, and the latter can accurately learn and compensate for gravity that is mainly caused by the attached external arthroscope. The right-arm robot is implemented with the point-based VF generation algorithm which can generate VF directly from point clouds with any shape, and rendering and providing VF force feedback to the operator as haptic clues. Since both the left-arm robot and right-arm robot in our prototype are haptic devices, the right-arm robot does not require a user-defined controller when implementing the point-based VF algorithm, and it can also provide haptic feedback with high fidelity. As shown in Fig. 1c, the VF, force feedback, and surgical tools are visualized in Unity to provide additional visual feedback to the operator.

As shown in the prototype of Fig. 1b, some connectors are designed and 3D-printed for the left-arm robot and the right-arm robot in order to attach the surgical instruments (*e.g.*, the arthroscope, and the handheld surgical bur) to the robot EEs. Especially, to attach the handheld bur to the right-arm robot, 3D scanning on the handheld bur is conducted first, and then the 3D model of the handheld bur having an ergonomic shape design is used to design the connector. The surgical instruments (arthroscope and surgical burs) and designed connectors are illustrated in Fig. 3.

It is worth noting that for the right-arm robot, the surgical tool is rigidly mounted to the robot EE (a cylindrical handle bar) via the customized 3D-printed connector and bolts-nuts as shown in Fig. 3b. The connector is deliberately designed to connect to the robot EE through an interference fit joint, thus no slippages can occur. The tool tip is then calibrated to be the new robot EE via the robot kinematics.

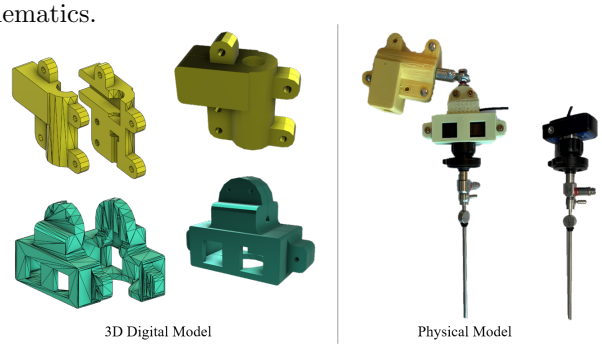

(a) Arthroscope

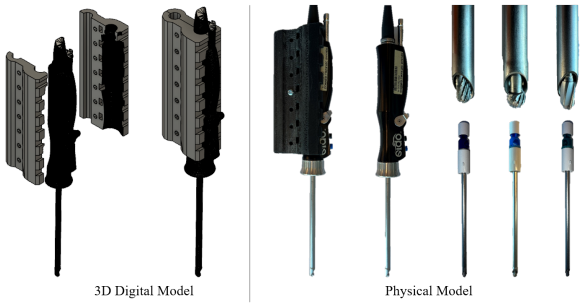

(b) Surgical burs

Fig. 3: Connectors and surgical instruments.

The dual-arm configuration of our prototype is designed to mimic the coordination between a surgeon's two hands while exercising dexterity and control, which is vital in navigating the surgical tools in the confined spaces during arthroscopic surgery, while providing haptic feedback as additional haptic assistance. With the left-arm robot-assisted arthroscope holder, the surgeon's hand will be freed

to focus on some other more important tasks, and when necessary the surgeon can easily operate the arthroscope via a pedal switch. With the right-arm robot-assisted surgical tool with haptic feedback, surgeons can have a lower cognitive load and higher confidence when navigating the tool in confined spaces and conducting dexterous operation procedures. With additional 3D visual feedback, the surgeon can easily figure out where the tooltip is located in the big picture during the surgery.

3. Experimental Evaluation on the Prototype

In this section, we conducted a series of experimental tests to evaluate the prototype of the proposed two-arm system in conditions simulating arthroscopic surgical environments. Note that we conducted the evaluations on the left-arm robot and the right-arm robot respectively since the functions and control systems of the two robots are independent although they work collaboratively in the surgical scenario. This also ensures the evaluation goals are clear and focused for each robot.

We configure the two-arm system to replicate common surgical tasks, with the left-arm robot holding an arthroscope and providing an arthroscope view through the camera-like device, and the right-arm robot manipulating a surgical bur. These tests are meant to evaluate the system's precision, responsiveness, and ability to handle complex maneuvers typical of joint arthroscopic surgeries. The following sections detail each experiment, outlining the setup, execution, and specific objectives aligned with our research goals in advancing robotic-assisted arthroscopic surgery.

3.1. *Robotic System of the Prototype*

A prototype of a two-arm robot-assisted arthroscopic surgical system is constructed and illustrated in Fig. 1. A pair of 6DOF Quanser's High Definition Haptic Device (HD^2) robots (Quanser Inc., Markham, ON, Canada), PY (positive y-axis) robot and NY (negative y-axis) robot are used as the left-arm robot and the right-arm robot, respectively, as illustrated in Fig. 1. Note that the two robots have different definitions on the base frame, as shown in the figure. A relevant kinematics analysis of the HD^2 PY robot is available in [25]. The Cartesian workspace of each of the HD^2 robots is $[x, y, z, roll, pitch, yaw]$: $[800mm, 250mm, 350mm, 180°, 180°, continuous]$. The HD^2 robot highlights its features on large workspace and very low intervening dynamics, as well as highly backdrivable joints with negligible friction due to the parallel mechanism design. For more details on their kinematic features, please refer to the system specifications[a]. It is noteworthy that the large workspace and the kinematic design of the robotic arms help to accommodate the range of motion required in arthroscopic surgery, and it allows the arms to replicate the complex movements of a surgeon's hands within the constrained space of an arthroscopic procedure. In this work, the two robots are controlled via joint torque commands, which are sent from MATLAB/Simulink (version R2016a, MathWorks Inc., Natick, MA, USA) using Quarc real-time control software (Quanser Inc., Markham, ON, Canada). The control rate of the robot is $1,000$ Hz. The MATLAB/Simulink and Quarc software run on a computer with a 3.20 GHz Intel(R) Core(TM) i5-3470 CPU with a Windows 7 Enterprise 64-bit operating system.

In the prototype, as shown in Fig. 1, the left-arm robot EE is attached to an arthroscope (Sawbones®, A Pacific Research Company, Vashon Island, Washington, USA) via one customized 3D-printed connector, while the right-arm robot EE is attached to a handheld surgical bur (Ergo™ Shaver Handpiece, CONMED LINVATEC SHAVER, Linvatec Corporation, Largo, Florida, USA) via another customized 3D-printed connector. A modified FAST (fundamentals of arthroscopic surgery training) simulator (Sawbones®, A Pacific Research Company, Vashon Island, Washington, USA) is used as a platform for an arthroscopic surgery mockup, while a soap block with a size of $22 \times 88 \times 48$mm is used to represent the bone.

The two robots work independently but collaboratively in the proposed prototype. The left-arm robot is used as a robotic arthroscope holder which can hold the arthroscope still for the surgeon and prevent external disturbances. Its position can be adjusted when the surgeon needs to change the arthroscope view perspective. This is realized by a pedal, *i.e.*, when the pedal is unpressed (default), the arthroscope will be held still by the robot (interaction disabled in the robot control system), and when the pedal is pressed, the arthroscope can be moved to a new position (interaction enabled in the robot control system). The right-arm robot is attached to a surgical instrument at its EE, and the surgeon can conduct the surgery via the handheld surgical instrument. During the surgery, the pose (position and rotation) of the instrument will be tracked in real-time by the robot, and visualized in Unity (version 2022.3.11f1, Unity Technologies, San Francisco, CA, USA). Moreover, a VF generated from a customized point cloud[19] is also visualized in Unity, and it is designed to help the surgeon remove the extra bone based on a preoperative plan and provide haptic feedback to the surgeon.

In the control block diagram of the prototype, as illustrated in Fig. 2, a Git scheme is implemented with an impedance controller in the left-arm robot, where the former can accurately learn and compensate for gravity while the latter can ensure compliant robot behavior during physical human-robot interaction (pHRI). On the other hand, an algorithm of a point-based 3D VF-generating method[19] is implemented in the right-arm robot. With the VF algorithm, the operator can receive force feedback as additional haptic assistance when the surgical instrument is in contact

[a]Quanser: https://www.quanser.com/products/hd2-high-definition-haptic-device/

with the VF. The communications between the right-arm robot and Unity are realized by user datagram protocol (UDP) at a rate of 100 Hz, where the real-time pose of the right-arm robot EE is sent to Unity for visualization.

3.2. *Parameterization*

For all the experiments in this work, the parameter values used in the controller and algorithms are listed in Table 1. In the following sub-sections, a series of experiments are conducted to evaluate the effectiveness of the proposed prototype of a two-arm robot-assisted arthroscopic surgical system. Note that the two robots are evaluated individually since they work independently despite being collaboratively in the system. The demonstrations of the experiments can be found in the supplementary video.[b]

Table 1: Parameterization for the experiments.

Robot	Parameter	Assigned Value
L	spring gain	$\mathbf{K_m = 400I}$
L	damper gain	$\mathbf{D_m = 40I}$
L	Git gain γ	1
L	learning rate η	0.001
R	VF force gain k_{vf}	500
R	VF sphere r_{vf}	0.002 m
R	VF r_c	0.005 m
R	VF r_1	0.00049 m
R	VF r_2	0.00501 m
R	VF r_3	0.010 m
R	VF sine wave points	$N = 30351$
R	VF sine wave px	$[-0.3, 0.1]$ m, step=0.002
R	VF sine wave py	$[-0.5, -0.2]$ m, step=0.002
R	VF sine wave pz	$pz = 0.03\sin(\frac{2\pi}{0.1}(py + \frac{0.1}{2})) - 0.2$
-	bone block points	$N = 13500$
-	bone block size	$x \times y \times z = 0.022 \times 0.088 \times 0.048$ m

Note: $\mathbf{I} \in \mathbb{R}^{3\times3}$ denote identity matrix. L, left-arm robot; R, right-arm robot; Git, gravity iterative learning scheme; VF, virtual fixture. The tunable gains are determined via trial and error with a binary search strategy. Note that for the left-arm robot, all four experiments share the same set of impedance gains for a fair comparison across the experiments.

3.3. *Left-Arm Evaluation: Holding the Arthroscope*

The left-arm robot is evaluated by four experiments. The evaluation aim is to show that, by implementing the impedance controller and Git scheme, the robot can hold the arthroscope still (interaction disabled), while if needed, the robot allows the operator to adjust the scope view perspective (interaction enabled) via a pedal switch. In other words, when the pedal is unpressed ($Pedal = 0$, in regulation mode, default), the robot EE keeps the position still while rejecting any disturbances; when the pedal is pressed ($Pedal = 1$, default, in pHRI mode), the robot allows the operator to move the robot EE freely. The experiment setup for the left-arm robot is shown in Fig. 4. Note that when the robot EE keeps the position still in the setpoint regulation mode, the robot will behave like a stiff spring if any accidental short disturbance (*e.g.*, user-applied force) is applied onto the robot EE, and the stiffness level can be tuned via the impedance gains for robustness. This ensures a safe human-robot interaction (expected or unexpected) through compliant robot behavior.

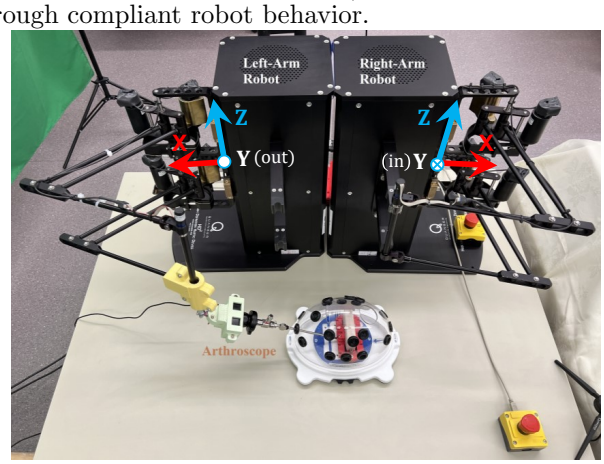

Fig. 4: Left-arm robot experiment setup.

More specifically, Experiment 1 aims to evaluate the control accuracy of only an impedance controller. Experiment 2 aims to evaluate the control accuracy of only an impedance controller when a heavy external payload is attached to robot EE. Experiment 3 aims to evaluate the capabilities of the Git scheme to learn and compensate for the heavy external payload. The objective of Experiment 4 is to evaluate the precision, stability, and control capabilities of the prototype in mimicking a robot-assisted arthroscopic holder.

In Experiment 1 of the left-arm robot (L-Exp.1), nothing is attached to the robot EE. The robot is implemented with only an impedance controller (reduced to a PD controller in pHRI scenario). The result of L-Exp.1 is shown in Fig. 5. As can be seen in the figure, when the pedal is unpressed ($Pedal = 0$), the robot EE position can be accurately regulated, while when the pedal is pressed ($Pedal = 1$), the robot EE position is allowed to move freely. Noticed that in the yellow-colored area, when the pedal is pressed ($Pedal = 1$) but human-robot interaction is not involved, the robot EE will drift downward slowly as indicated by the red line due to inaccurate gravity compensation.

In Experiment 2 of the left-arm robot (L-Exp.2), nothing is attached to the robot EE at the beginning, and an external payload (515g) is attached to the robot EE during the task (18∼60s). Same as the L-Exp.1, the robot is implemented with only an impedance controller. The result of

[b]Online video link: https://drive.google.com/file/d/1l4FpUsMlJz-OLZvaLOPKG9Lvdwqlwb2p/view?usp=sharing

L-Exp.2 is shown in Fig. 6. Similar to the result of L-Exp.1, when the pedal is unpressed ($Pedal = 0$), the robot EE position can still be effectively regulated even with a heavy payload (515g) attached (18∼60s), while when the pedal is pressed ($Pedal = 1$), the robot EE position is allowed to move freely. However, as can be observed in Fig. 6a, the actual positions shift downward a bit (along z-axis) compared to the desired ones in regulation mode ($Pedal = 0$), revealing a relatively lower regulation accuracy than that in L-Exp.1 due to the uncompensated payload. Moreover, as indicated in the yellow-colored area, when the pedal is pressed ($Pedal = 1$) but human-robot interaction is not involved, the robot EE will drift downward quickly to the ground as indicated by the red line due to the heavy yet uncompensated payload (515g). The quick-dropping process is more clearly reflected in Fig. 6b during which the commanded force is remarkably affected with a short oscillation occurred.

In Experiment 3 of the left-arm robot (L-Exp.3), the task is similar to that in L-Exp.2, *i.e.*, nothing is attached to the robot EE at the beginning, and an external payload (515g) is attached to the robot EE during the task (20∼60s). Different from L-Exp.1 and L-Exp.2, the robot in L-Exp.3 is implemented with an additional Git scheme for gravity learning and compensation. The result of L-Exp.3 is shown in Fig. 7. Similarly, when the pedal is unpressed ($Pedal = 0$), the robot EE position can be accurately regulated even with a heavy payload (515g) attached (20∼60s), while when the pedal is pressed ($Pedal = 1$), the robot EE position is allowed to move freely. Interestingly, as indicated in the yellow-colored area, when the pedal is pressed ($Pedal = 1$) but human-robot interaction is not involved, the robot EE does not drift downward anymore due to the Git scheme having accurately learned and compensated for the gravity (see Fig. 7b). Note that here the yellow-colored area involves physical human-robot interaction as well. Additionally, it is worth noting that the Git scheme revealed a quick and smooth convergence process during 20∼25s immediately after the heavy payload attached to the robot EE.

In Experiment 4 of the left-arm robot (L-Exp.4), the robot EE is attached with an arthroscope (713g), and the robot is implemented with a Git scheme for gravity compensation in addition to an impedance controller, which is the same as that in L-Exp.3. The result of L-Exp.4 is shown in Fig. 8. As shown in the figure, when the pedal is unpressed ($Pedal = 0$), the robot EE position (*i.e.*, the arthroscope) can be accurately regulated, while when the pedal is pressed ($Pedal = 1$), the robot EE position is allowed to move freely to adjust the arthroscope view perspective. This evaluated the effectiveness of the left-arm robot for holding with the arthroscope. It is worth noting that Fig. 8b revealed another quick and smooth convergence process during 0∼10s which demonstrated the stability of the Git scheme in the transient process of converging.

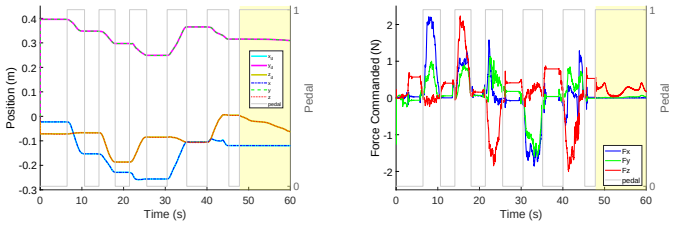

(a) Position (b) Force Commanded

Fig. 5: Experiment result of L-Exp.1 in *p*HRI scenario with only an impedance controller implemented. Note that the yellow-colored area corresponds to the *p*HRI mode ($Pedal = 1$) but no *p*HRI occurring.

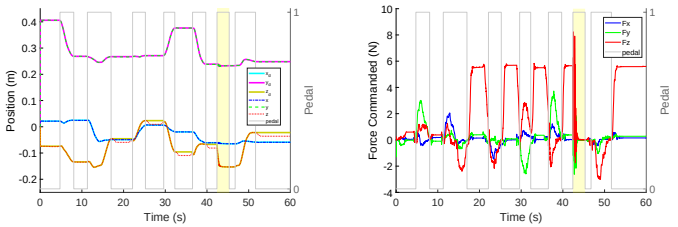

(a) Position (b) Force Commanded

Fig. 6: Experiment result of L-Exp.2 in *p*HRI scenario with only an impedance controller implemented, while an extra payload (515g) attached to the robot EE. Note that the yellow-colored area corresponds to the *p*HRI mode ($Pedal = 1$) but no *p*HRI occurring.

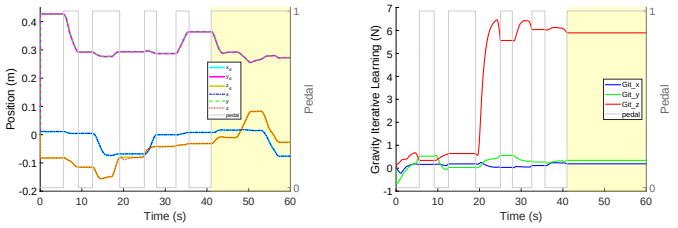

(a) Position (b) Git Iterative Learning

Fig. 7: Experiment result of L-Exp.3 in *p*HRI scenario with an impedance controller and Git scheme implemented, while an extra payload (515g) is attached to the robot EE. Note that the yellow-colored area corresponds to the *p*HRI mode ($Pedal = 1$), and both *p*HRI and non-*p*HRI are involved.

In summary, the results from L-Exp.1 indicate that an impedance controller can provide robot compliance, but the control accuracy can be potentially affected by uncompensated gravity. The findings of L-Exp.2 emphasize the results of L-Exp.1 more clearly that an impedance controller alone is not capable of dealing with heavy external payloads when mimicking a heavy arthroscope attached to the robot EE. In regulation mode, the uncompensated heavy payload will lower the regulation accuracy, while in *p*HRI mode, the uncompensated heavy payload will drive the robot EE to drop

toward the ground if there is no human-robot interaction involved. The outcomes of L-Exp.3 help validate the capability of the Git scheme to compensate for the heavy payload gravity. In regulation mode, the regulation accuracy can be recovered to a high level, while in *p*HRI mode, the robot EE attached with a heavy payload can stay in the air even if there is no human-robot interaction involved, and all of those are due to the payload is accurately compensated by the Git scheme. The results of L-Exp.4 validate and support our primary goal on system accuracy and stability of the robot-assisted arthroscope holder.

It is worth mentioning that during human-robot interaction (in *p*HRI mode) in physical experiments, the joint friction, although negligible but existent, may appear and be perceived by the operator mixing with the damping force from the impedance model. But it will not affect the whole system's stability and accuracy. In the steady state of set-point regulation mode, the joint friction will disappear, while this steady state is the one the left-arm robot will remain in for most of the time during the surgery.

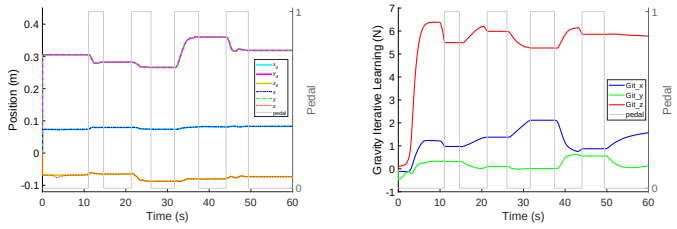

(a) Position (b) Git Iterative Learning

Fig. 8: Experiment result of L-Exp.4 in *p*HRI scenario with an impedance controller and Git scheme implemented, while an arthroscope (713g) is attached to the robot EE.

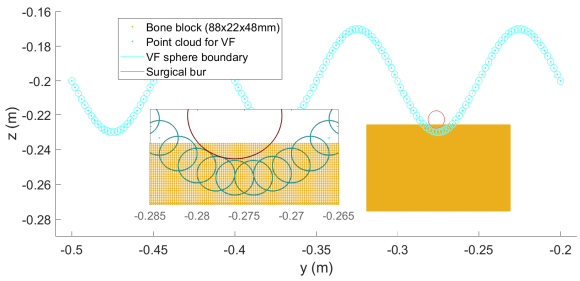

(a) Registration

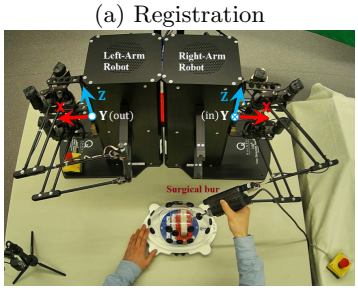

(b) Setup

Fig. 9: Right-arm robot experiment setup and VF-bone registration.

3.4. *Right-Arm Evaluation: Burring Bone with VF*

The right-arm robot is implemented with a point-based VF algorithm where the VF can be generated directly from a point cloud with any shape.[19] Here in this work, a point cloud of a sinusoidal wave is employed as shown in Fig. 9a. In the figure, the brown rectangular area represents a bone block, while the red circle represents the surgical bur. The bone above the sine wave needs to be removed during the task. As shown in Fig. 9b, a surgical bur is attached to the right-arm robot EE which is used to remove the extra bone. The detailed parameterization related to the point cloud is summarized in Table 1.

The VF, surgical bur, and bone block are also visualized in Unity in real-time during the task as illustrated in Fig. 1c. The evaluation aim for the right-arm robot is to show that, by implementing the point-based VF algorithm, the VF can provide force feedback to the operator during surgery operations (*e.g.*, extra bone removal), thus assist the operator in bone-removing with both haptic cues and visualization together. In order to ensure the bone block is burred based on the designed VF as illustrated in Fig. 9a, a VF-bone registration needs to be done. The procedures for VF-bone registration we used are the following, (1) the bone is stably fixed on an experimental platform (*i.e.*, the FAST simulator shown in Fig. 9b); (2) the platform is then stably fixed at an appropriate location within the robot workspace; (3) the bone position coordinates in the robot workspace can then be retrieved via the robot EE (*i.e.*, the tool tip); (4) the VF is then registered such that the VF valley penetrates into the top side of the bone for 3 mm along z-axis as illustrated in Fig. 9a. It is worth mentioning that the VF-bone registration method we used has a main focus on the z-axis registration. However, the actual burring depth by the bur along the z-axis still will be affected by the user-configured stiffness of the VF, *e.g.*, a "soft" VF will allow bigger burring depth while a "stiff" VF will allow smaller burring depth.

There are two experiments designed for evaluating the right-arm robot. The first experiment (R-Exp.1) is to conduct a bone-removing task in an open space (mimicking open surgery) where the cover of the FAST simulator is removed (see Fig. 10), while the second experiment (R-Exp.2) is to conduct the same bone-moving task via a small portal (mimicking MIS) where the cover of the FAST simulator is involved (see Fig. 9b).

A probing test on the right-arm robot is performed first based on R-Exp.1 as shown in Fig. 10. Some scenario diagrams for typical procedures are also presented in the figure. Scenario ① is in preparation stage. Scenario ② is in a VF probing and force feedback test, where the goal is to test the VF force rendering as well as its visualization in Unity. Scenario ③ is in a VF outline probing test, where the goal is to detect the sinusoidal outline of the VF. Scenario ④ and ⑤ are in a VF valley probing test, where the goal is to move along the valley of the VF. Scenario ④ is

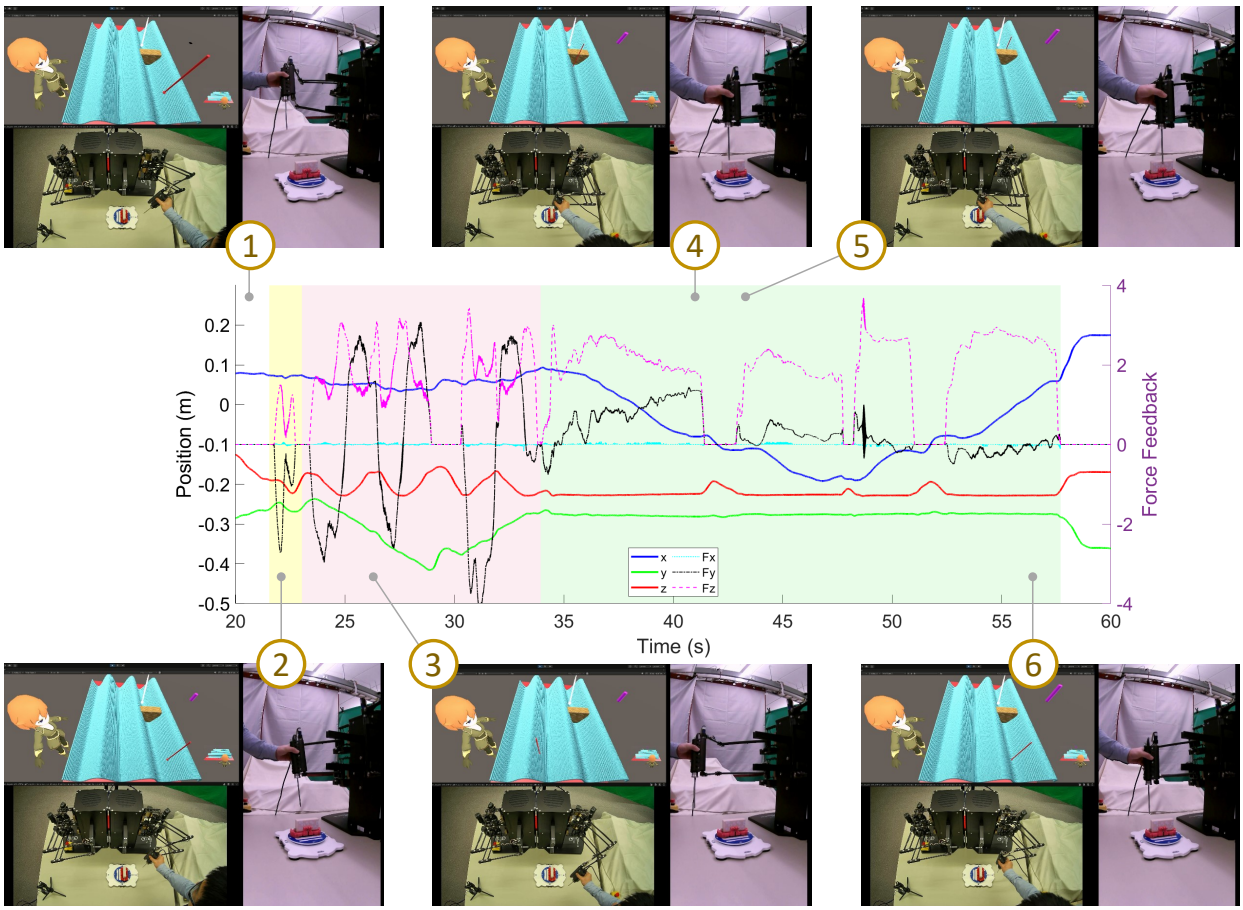

Fig. 10: Probing test result of R-Exp.1 in *p*HRI scenario with an algorithm of point-based VF implemented, while a handheld surgical bur (435g) is attached to the robot EE. Scenario ①, preparation stage; Scenario ②, VF probing and force feedback test; Scenario ③, VF sinusoidal outline probing test; Scenario ④ ⑤, VF valley probing test; Scenario ⑥, ending stage.

on one side of the bone block, and scenario ⑤ is on the other side of the bone block. Scenario ⑥ is in an ending stage. The probing test results show that the VF force can be appropriately rendered and delivered to the operator, and the VF, surgical bur, and force feedback values are also correctly visualized in Unity.

In traditional MIS elbow arthroscopy, the surgeon removes the osteophytes under the arthroscope view, and the actual amount of the bone to be removed mainly relies on the surgeon's experience and the memorized preplan in the surgeon's brain. The right-arm robot can assist the surgeon in removing bone that is bound by surgeon-defined VF, while providing haptic feedback to the surgeon to indicate where the VF boundary is. Therefore, the goal of the bone-burring task in this work is to remove the bone bounded by the VF as illustrated in Fig. 9a.

The bone-burring task results of R-Exp.1 and R-Exp.2 are shown in Fig. 11a and Fig. 11b, respectively. As can be seen in the figure, both experiments of R-Exp.1 and R-Exp.2 can generate relatively good bone-burring task performance with the VF assistance. In other words, the bone-burring task can be effectively conducted with the right-arm robot either in simulated open surgery (Fig. 11a) or in simulated MIS surgery (Fig. 11b), although the former results in a relatively smooth and a bit wider bone-burring surface than the latter. This is reasonable since the latter of MIS surgery is performed via a restricted portal. These results evaluated the effectiveness of the right-arm robot including the point-based VF generation algorithm, VF force rendering, haptic feedback, and visualization in Unity. Note that for the bone-burring task results, we provide a qualitative result rather than a quantitative result, this is because the quantitative performance heavily depends on the parameter configuration when setting the force rendering of the VF, *i.e.*, when a "soft" VF is configured, more bone material will be removed than planned since higher penetration to the VF boundary is allowed, while on the contrary,

when a "stiff" VF is configured, few more bone material will be removed than planned since low penetration to the VF boundary is allowed.

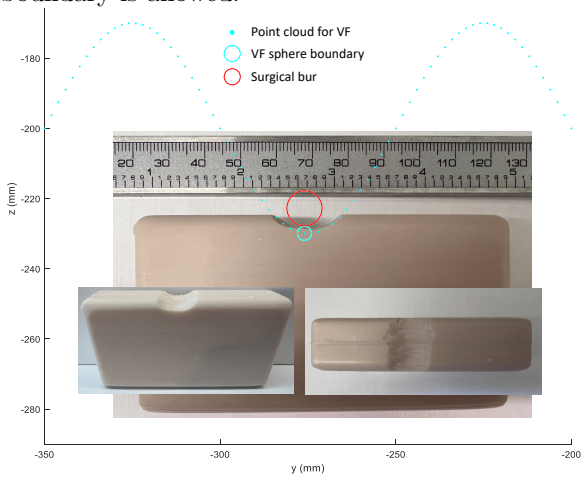

(a) R-Exp.1 in open surgery scenario

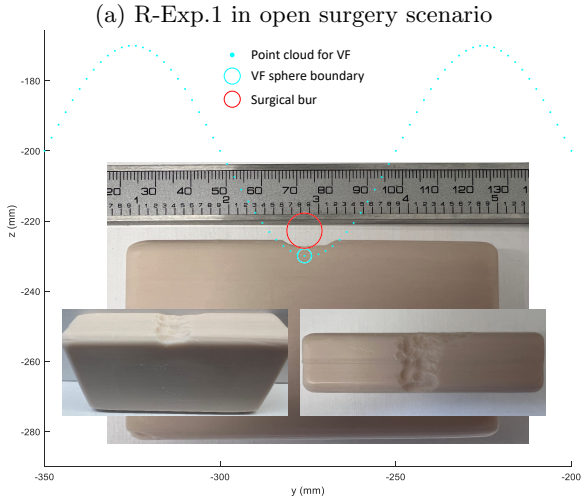

(b) R-Exp.2 in MIS surgery scenario

Fig. 11: Experiment results of R-Exp.1 and R-Exp.2. The bone is represented by a soap block with a size of $22 \times 88 \times 48$mm.

3.5. *Future Work*

In surgical scenarios, safety is of paramount importance. For the left-arm robot in the proposed robot-assisted system, a safe and compliant human-robot interaction can be ensured by the impedance controller, which can guarantee compliant robot behavior. For the right-arm robot, since VF assistance and haptic feedback are the main features, the safety of human-robot interaction solely relies on the stability and reliability of the VF algorithm, which has been systematically verified in our previous work [19]. On the other hand, system accuracy is another main concern. The Git scheme implemented in the left-arm robot can guarantee accurate regulation through accurate gravity estimation and compensation, while the performance accuracy of the right-arm robot relies on the user-configured stiffness of the VF.

For the bone-burring tasks conducted via the right-arm robot, we provided only qualitative performance results as introduced earlier. In future work, we will make a more deliberate experimental design such that the experimental results can be evaluated quantitatively. For example, we can reconstruct the 3D digital models of the bone before and after the surgical operations, and then make a comparison quantitatively. We can also design an experiment to compare the task performance with and without VF assistance, to evaluate to what extent the VF assistance and haptic feedback can help to improve the task performance.

There are some other aspects that can be improved in future work. First, the two robots work independently despite collaboratively in this work. To visualize the real-time position of the left-arm robot in Unity, it needs to be registered into the same coordinate system as the right-arm robot. Second, the bone is represented by a soap block which could have different stiffness of material properties from the bone. A real bone would be used in future work. Third, the registration of the bone into the right-arm robot workspace is only conducted along the vertical z-axis as a simplified case. In future work, full registration of a real bone should be conducted along all three Cartesian axes. Additionally, a preplanned image-based surgical scenario can be also involved. The inclusion of preoperative images would allow for more precise mapping of the surgical field and enable the robot to navigate and interact with the patient's anatomy with a higher degree of fidelity. Last but not least, the experiments in this work are dry experiments without fluid filling around the bone. In future work, wet experiments should be designed for more realistic arthroscopic surgeries.

Some other improvements can be made in future work. For example, the miniaturization of the components of the connectors between robot and surgical tool, enhancing the additional 3D visual feedback by introducing augmented reality (AR) techniques, and designing more realistic and more complex surgical scenarios where robotic assistance can make a difference.

4. Conclusions

In this paper, a prototype of a two-arm robot-assisted arthroscopic surgical system is presented. The system is composed of a pair of haptic devices. The left-arm robot is attached to an arthroscope while the right-arm robot is attached to a handheld surgical bur. The left-arm robot is implemented with an impedance controller and a Git scheme, where the former ensures a safe human-robot interaction while the latter accurately learns and compensates for gravity. The right-arm robot is implemented with a point-based VF generation algorithm, which can generate VF directly from point clouds with any shape. A series of experiments are conducted to evaluate the effectiveness of

the prototype system. The results show that the left-arm robot can effectively hold the arthroscope still and allow the operator to move the arthroscope via a pedal switch whenever needed, and the right-arm robot can render appropriate VF force feedback from the VF algorithm and deliver it to the operator as haptic assistance. Also, the VF, the bone, and the surgical bur with its real-time position are visualized in Unity to provide additional visual feedback to the operator.

Debridement of osteophytes is a specific example surgery we used to evaluate the prototype in this work, and it is a small arthroscopic surgery that is common in the elbow and hip. Beyond this, the proposed prototype is promised to be used in a wide variety of arthroscopic surgeries in orthopedics including (1) soft tissue repair/reconstruction, which is most commonly happened in the shoulder (*e.g.*, rotator cuff repair, labral repair) and the knee (*e.g.*, anterior cruciate ligament (ACL) repair/reconstruction, meniscal repair), and these are by far the most common applications of arthroscopy in orthopedics based on the volume of work, but there is also some interest in elbow recently for ligament augmentation, repair/reconstruction; (2) bony debridement, which is commonly happened in elbow (osteophytes), hip, and shoulder (distal clavicle excision); (3) trauma, *e.g.*, fracture reduction/fixation, *etc.* With the robotic assistance of the proposed two-arm system, it is expected to help increase the surgeon's accuracy and reliability while reducing invasiveness.

The implications of this work can extend beyond orthopedics, suggesting wider applicability of such advanced robotic systems in various medical fields. The development and successful evaluation of our prototype underline the potential for more precise, controlled, and ergonomic surgical procedures using similar concepts derived from impedance control for robot compliance, a Git scheme for gravity compensation, and a point-based VF generation algorithm for objects in any shape.

Acknowledgments

This research is supported in part by the Canada Foundation for Innovation (CFI) under grants LOF 28241 and JELF 35916, in part by the Government of Alberta under grants IAE RCP-12-021 and EDT RCP-17-019-SEG, in part by the Government of Alberta's grant to Centre for Autonomous Systems in Strengthening Future Communities (RCP-19-001-MIF), in part by the Natural Sciences and Engineering Research Council (NSERC) of Canada under grants RTI-2018-00681, RGPIN-2019-04662, and RGPAS-2019-00106, and in part by the Edmonton Civic Employee Charitable Assistance Fund.

References

[1] T. Li, A. Badre, F. Alambeigi, and M. Tavakoli, "Robotic systems and navigation techniques in orthopedics: A historical review," *Applied Sciences*, vol. 13, no. 17, p. 9768, 2023.

[2] M. G. Fujie and B. Zhang, "State-of-the-art of intelligent minimally invasive surgical robots," *Frontiers of Medicine*, vol. 14, no. 4, pp. 404–416, 2020.

[3] K. Bennett and S. Kamineni, "History of elbow arthroscopy," *Journal of Arthroscopic Surgery and Sports Medicine*, vol. 1, no. 1, pp. 23–31, 2020.

[4] T. Li, A. Badre, H. D. Taghirad, and M. Tavakoli, "Integrating impedance control and nonlinear disturbance observer for robot-assisted arthroscope control in elbow arthroscopic surgery," in *2022 IEEE/RSJ International Conference on Intelligent Robots and Systems (IROS)*. IEEE, 2022, pp. 11 172–11 179.

[5] ——, "Neural network learning of robot dynamic uncertainties and observer-based external disturbance estimation for impedance control," in *2023 IEEE/ASME International Conference on Advanced Intelligent Mechatronics (AIM)*. IEEE, 2023, pp. 591–597.

[6] T. Li, A. Zakerimanesh, Y. Ou, and M. Tavakoli, "Iterative learning for gravity compensation in impedance control," *IEEE/ASME Transactions on Mechatronics*, pp. 1–12, 2024.

[7] T. Li, H. Xing, E. Hashemi, H. D. Taghirad, and M. Tavakoli, "A brief survey of observers for disturbance estimation and compensation," *Robotica*, vol. 41, no. 12, pp. 3818–3845, 2023.

[8] T. Xia, A. Kapoor, P. Kazanzides, and R. Taylor, "A constrained optimization approach to virtual fixtures for multi-robot collaborative teleoperation," in *2011 IEEE/RSJ International Conference on Intelligent Robots and Systems*. IEEE, 2011, pp. 639–644.

[9] T. L. Gibo, L. N. Verner, D. D. Yuh, and A. M. Okamura, "Design considerations and human-machine performance of moving virtual fixtures," in *2009 IEEE International Conference on Robotics and Automation*. IEEE, 2009, pp. 671–676.

[10] S. Park, R. D. Howe, and D. F. Torchiana, "Virtual fixtures for robotic cardiac surgery," in *International conference on medical image computing and computer-assisted intervention*. Springer, 2001, pp. 1419–1420.

[11] F. Ryden and H. J. Chizeck, "Forbidden-region virtual fixtures from streaming point clouds: Remotely touching and protecting a beating heart," in *2012 IEEE/RSJ International Conference on Intelligent Robots and Systems*. IEEE, 2012, pp. 3308–3313.

[12] ——, "A proxy method for real-time 3-DOF haptic rendering of streaming point cloud data," *IEEE transactions on Haptics*, vol. 6, no. 3, pp. 257–267, 2013.

[13] S. Nia Kosari, F. Rydén, T. S. Lendvay, B. Hannaford, and H. J. Chizeck, "Forbidden region virtual fixtures from streaming point clouds," *Advanced Robotics*, vol. 28, no. 22, pp. 1507–1518, 2014.

[14] M. M. Marinho, H. Ishida, K. Harada, K. Deie, and M. Mitsuishi, "Virtual fixture assistance for suturing in robot-aided pediatric endoscopic surgery," *IEEE Robotics and Automation Letters*, vol. 5, no. 2, pp.

524–531, 2020.

[15] M. Selvaggio, G. A. Fontanelli, F. Ficuciello, L. Villani, and B. Siciliano, "Passive virtual fixtures adaptation in minimally invasive robotic surgery," *IEEE Robotics and Automation Letters*, vol. 3, no. 4, pp. 3129–3136, 2018.

[16] R. Moccia, C. Iacono, B. Siciliano, and F. Ficuciello, "Vision-based dynamic virtual fixtures for tools collision avoidance in robotic surgery," *IEEE Robotics and Automation Letters*, vol. 5, no. 2, pp. 1650–1655, 2020.

[17] R. Johansson, I. Santelices, D. O'Connell, M. Tavakoli, and D. Aalto, "Evaluation of the use of haptic virtual fixtures to guide fibula osteotomies in mandible reconstruction surgery," in *2019 IEEE 15th International Conference on Automation Science and Engineering*, 2019.

[18] L. Cheng, J. Carriere, J. Piwowarczyk, D. Aalto, N. Zemiti, M. de Boutray, and M. Tavakoli, "Admittance-controlled robotic assistant for fibula osteotomies in mandible reconstruction surgery," *Advanced Intelligent Systems*, vol. 3, no. 1, p. 2000158, 2021.

[19] T. Li, A. Badre, H. D. Taghirad, and M. Tavakoli, "Point-based 3D virtual fixture generating for image-guided and robot-assisted surgery in orthopedics," in *2023 IEEE/ASME International Conference on Advanced Intelligent Mechatronics (AIM)*. IEEE, 2023, pp. 179–186.

[20] J. Fong, H. Rouhani, and M. Tavakoli, "A therapist-taught robotic system for assistance during gait therapy targeting foot drop," *IEEE Robotics and Automation Letters*, vol. 4, no. 2, pp. 407–413, 2019.

[21] S. Bruno, S. Lorenzo, V. Luigi, and O. Giuseppe, *Robotics: modelling, planning and control*. Spinger, 2010.

[22] P. Song, Y. Yu, and X. Zhang, "A tutorial survey and comparison of impedance control on robotic manipulation," *Robotica*, vol. 37, no. 5, pp. 801–836, 2019.

[23] A. De Luca and S. Panzieri, "A simple iterative scheme for learning gravity compensation in robot arms," in *Proc. Ann. Conf. ANIPLA*, 1992.

[24] C. B. Zilles and J. K. Salisbury, "A constraint-based god-object method for haptic display," in *Proceedings 1995 ieee/rsj international conference on intelligent robots and systems. Human robot interaction and cooperative robots*, vol. 3. IEEE, 1995, pp. 146–151.

[25] L.-F. Lee, M. S. Narayanan, F. Mendel, V. N. Krovi, and P. Karam, "Kinematics analysis of in-parallel 5 dof haptic device," in *2010 IEEE/ASME International Conference on Advanced Intelligent Mechatronics*. IEEE, 2010, pp. 237–241.

Teng Li received the M.E. degree in mechanical manufacturing and automation from the Tianjin University of Science and Technology, Tianjin, China, in 2014 and the Ph.D. degree in mechanical design and theory from Beihang University, Beijing, China, in 2019. He is currently working toward the Ph.D. degree in electrical and computer engineering with the University of Alberta, Edmonton, AB, Canada. His research interests include surgical robotics, robot control systems, physical human-robot interaction, and haptics.

Armin Badre received the graduation degree from the Faculty of Medicine, University of Alberta, Edmonton, AB, Canada, in 2012, and the M.Sc. degree in surgery, with a focus on elbow biomechanics, from Roth McFarlane HULC, London, ON, Canada, in 2019.

In 2017, he completed his Orthopaedic Surgery training at the University of Alberta. Upon graduation, he went to the Roth McFarlane HULC, a world-renowned upper extremity specialized center, to subspecialize in the management of complex elbow, hand, and wrist reconstruction and trauma.

He joined the Western Hand and Upper Limb Facility (WULF), Sturgeon Hospital, St. Albert, AB, in 2019. His clinical practice is focused on the management of various elbow, hand, and wrist conditions, including arthroscopy, arthroplasty, and upper extremity trauma. He has an academic appointment with the Faculty of Medicine, University of Alberta, and is involved with the teaching of medical students, residents, and fellows. He is quite keen on the advancement of knowledge through high-quality clinical and biomechanical research and is currently the research lead with WULF. He has authored or coauthored his work in a number of prestigious journals and presented at various national and international scientific meetings.

Mahdi Tavakoli received the Ph.D. degree in electrical and computer engineering from the University of Western Ontario, London, ON, Canada, in 2005.

He is currently a Professor with the Electrical and Computer Engineering Department and the Biomedical Engineering Department and a Senior University of Alberta Engineering Research Chair in Healthcare Robotics. He is also a Scientific Vice-Director for the Institute for Smart Augmentative and Restorative Technologies (iSMART), University of Alberta, Edmonton, AB, Canada. From 2006 to 2008, he was a Postdoctoral Researcher with Canadian Surgical Technologies and Advanced Robotics (CSTAR), London, ON, Canada, and an NSERC Postdoctoral Fellow with Harvard University, Cambridge, MA, USA. He is the lead author of *Haptics for Teleoperated Surgical Robotic Systems* (World Scientific, 2008) and the Specialty Chief Editor for *Frontiers in Robotics and AI* (Robot Design Section). His research interests involve medical robotics, image-guided surgery, and rehabilitation robotics.

Dr. Tavakoli is currently an Associate Editor for the *International Journal of Robotics Research*, *IEEE Transactions on Medical Robotics and Bionics*, *IEEE/ASME Transactions on Mechatronics*' Focused Section with Advanced Intelligent Mechatronics, and *Journal of Medical Robotics Research*.